Supporting Information

Oakes et al. 10.1073/pnas.1715869115

SI Materials and Methods

Cell Culture and Reagents. NIH 3T3 mouse fibroblasts (American Type Culture Collection) were cultured in DMEM (Mediatech, Inc.) supplemented with 10% FBS (HyClone; Thermo Fisher Scientific), 2 mM L-glutamine (Invitrogen), and penicillin–streptomycin (Invitrogen). Cells were tested for mycoplasma and were free of contamination. Cells were transiently transfected with a plasmid DNA construct encoding GFP–Stargazin (a gift from A. Karginov, University of Illinois at Chicago, Chicago). The following antibodies were used: mouse anti-Pxn and rabbit anti-p34 (Millipore); Cy5 donkey anti-mouse (Jackson ImmunoResearch Laboratories, Inc.); and Alexa Fluor 568 goat anti-rabbit (Invitrogen). Alexa Fluor 488 phalloidin was purchased from ThermoFisher Scientific. Blebbistatin was purchased from Sigma and used at a concentration of 50 μM. The Rho Kinase inhibitor Y-27632 was purchased from EMD Millipore and used at a concentration of 20 μM. The ARP2/3 inhibitor CK-869 and control compound CK-312 were purchased from Calbiochem and used at concentrations of 50 μM. The RGDs cyclo (Arg-Gly-Asp-D-Phe-Lys) and H-Arg-Gly-Asp-Ser-Lys-OH1 were purchased from Peptides International. Fibronectin derived from human plasma was purchased from Millipore. Vitronectin and collagen were purchased from Thermo Fisher Scientific. Mn^{2+} was purchased from Fischer Scientific and used at a concentration of 3 μM.

Polyacrylamide Substrates. Polyacrylamide (PA) substrates were prepared on glass coverslips by using published methods (1, 2). In brief, acrylamide/bis-acrylamide were used to create PA gels with Young's moduli of 0.6, 2.1, 4.5, 6.9, 8.4, 48, 90, and 150 kPa (1, 2). The 0.6- to 8.4-kPa gels were made with a 7.5% acrylamide solution, while the 48- to 150-kPa gels were made with 12% acrylamide solutions. Fibronectin, collagen, and RGDs were coupled to the surface of the PA gels by using the photoactivatable cross-linker sulfo-SANPAH (Thermo Fisher Scientific). PA gels were covered with a 2.5 mg/mL solution of sulfo-SANPAH and exposed to an 8-W UV lamp for 5 min. The PA gels were rinsed with PBS and incubated with 1 mg/mL fibronectin or RGD at room temperature for 45 min or in 2 mg/mL collagen at 4 °C overnight. The PA gels were then rinsed repeatedly and plated with cells. Vitronectin (ThermoFisher Scientific) was coupled to the surface of the PA gels via 1-ethyl-3-(3-dimethylaminopropyl)carbodiimide hydrochloride (EDC)/NHS chemistry (3, 4). Briefly, the polymerized gel was placed in a UVO-Cleaner 342 (Jelight) and illuminated with 185- and 254-nm UV light for 90 s. Gels were incubated in 200 μL of a solution containing 5 mg/mL EDC (Thermo Fisher Scientific) and 10 mg/mL NHS (Thermo Fisher Scientific) for 20 min. The EDC-NHS solution was then aspirated and replaced with a solution containing 10 μg/mL vitronectin in a buffer of Hepes (pH 8.5) for 20 min. Gels were washed three times for 5 min in PBS before cells were plated. Cells were plated on substrates for 2.5 h. CK compounds were added at plating, and blebbistatin, Y-27632, and manganese were added after 2 h unless otherwise noted.

Microscopy and Live Cell Imaging. Images were obtained by using Metamorph (Molecular Devices) acquisition software on either an Nikon Ti-E inverted microscope equipped with a metal halide light source (Lumen 200PRO; Prior Scientific) or a Nikon Eclipse Ti-E inverted microscope with a Yokogawa CSU-X1 confocal scanhead and Spectral Applied Research Laser Merge Module (491, 561, and 643 nm lasers). Images were obtained with a Photometrics Coolsnap HQ2 CCD camera using 20× Plan Fluor ELWD 0.45 NA, 40× Plan Fluor 1.3 NA, or 60× Plan Apo 1.2 NA objectives (Nikon). For live cell imaging, cells were mounted in a perfusion chamber (Warner Instruments) and maintained at 37 °C. Medium for live cell imaging was supplemented with 10 mM Hepes and 30 μL/mL Oxyrase (Oxyrase Inc.).

Immunofluorescence. Cells were rinsed in warm cytoskeleton buffer (10 mM Mes, 3 mM MgCl2, 1.38 M KCl, and 20 mM EGTA) and then fixed and permeabilized in 4% PFA (Electron Microscopy Sciences), 1.5% BSA (Thermo Fisher Scientific), and 0.5% Triton X-100 in cytoskeleton buffer for 15 min at 37 °C. Gels were then rinsed three times in PBS and incubated with mouse antipaxillin and rabbit anti-p34 (1:400; Millipore) for 1 h at room temperature. The gels were then rinsed three times in PBS before being incubated with fluorescently labeled secondary antibodies and phalloidin. Gels were rinsed three times and mounted in noncuring medium (SlowFade; Invitrogen) and sealed with nail polish.

Image Analysis. All image analysis was done by using ImageJ, MATLAB (MathWorks), or Python. Cell area was determined by thresholding images of actin to create binary masks. Protrusion analysis was performed by thresholding each image in a time series to create a binary mask, from which the cell contour could be extracted. Protrusive regions were identified by overlaying successive contours to identify regions of new area. Each protrusion was segmented to identify the total area, along with the leading and trailing edges. A given protrusion width was determined by taking each point along the leading-edge contour and determining the nearest distance to the trailing-edge contour and averaging across the entire set. The protrusion speed was calculated by dividing the average width by the frame interval of the time series.

To determine the location of intensity maxima for p34 and paxillin, images were first thresholded in the actin channel as described above to create a cell contour. We then performed a succession of one-pixel erosions, to create a series of contours that radially propagated toward the center of the cell. Lamellapodia regions were then identified and masked. To create linescans, we averaged the intensity signal in a window that was five contours in width (~0.5 μm) and shifted the window one contour toward the center of the cell for each step. This resulted in an average radial intensity from the edge of the cell. The distance plotted is the distance from the edge of the cell to the center of the window.

Traction Force Microscopy. Traction force microscopy was performed as described (4). Briefly, polyacrylamide gels were prepared as described above, but with the addition of 5 μL of 40-nm dark-red fluorescent microspheres (Invitrogen). Cells were micropatterned with circles of fibronectin (4). Cells were first imaged in normal medium supplemented with 10 mM Hepes and 30 μL/mL Oxyrase. The medium was then replaced with medium additionally supplemented with 3 μM Mn^{2+} and allowed to incubate for 30 min. Each cell was then imaged again. Finally, the cells were detached by using a 0.5% SDS solution, and the relaxed image of the gel was taken for each position. The traction forces were calculated by using the Fourier transform traction cytometry approach (5).

Computational Model

We used a Brownian Dynamics approach to simulate integrin binding and unbinding in response to differences in substrate stiffness. Integrins were represented as single point particles that

undergo cycles of diffusion, binding, and unbinding, along a quasi-2D surface mimicking the ventral surface of cells. The substrate was represented as an isotropic and elastic material, consisting of a bundle of ideal springs which mimic ligands. To simulate the effect of Mn^{2+} on integrin binding, we modulated the relationship of bond lifetime vs. force.

Computational Domain and Boundary Conditions. The computational domain is 3D and consists of two parallel surfaces: The bottom layer is fixed in space and represents the substrate (Fig. 5*B*); the top layer is an ideal surface, where integrin particles diffuse along x and y, with a diffusion coefficient of $D = 0.28\ \mu m^2/s$ (6). Integrin particles are harmonically restrained in the vertical direction, with an equilibrium distance, L, of 20 nm from the bottom layer. This distance between the integrin layer and substrate corresponds to the separation of the open extracellular integrin headpiece from the membrane (7). From the top, the computational domain is a square with side dimensions of 1 μm (Fig. 5*A*). To avoid finite size effects on integrin motion, we used periodic boundary conditions in the lateral directions, x and y.

Substrate Model. The substrate is an elastic solid, consisting of a bundle of ideal linear springs, with stiffness depending on the substrate rigidity, as:

$$k_{sub} = \frac{YA}{L},$$

where Y is the Young's modulus (we tested values in the range 2.1–16.8 kPa), A is the integrin/ligand cross-sectional area (corresponding to 80 nm^2, from an ideal bar of radius ~5 nm, corresponding to approximately half the value of the transmembrane leg separation of an integrin in the open conformation), and L is the equilibrium distance separation between substrate and top layer.

Hooke's law for each spring in the bundle can be written as:

$$\boldsymbol{F_{sub}} = k_{sub}\boldsymbol{\Delta L},$$

with $\boldsymbol{\Delta L}$ corresponding to the deviation from the equilibrium distance separation between the two surfaces. We used a spring density of 400 per μm^2. While the magnitude of the fraction of bound integrins at the steady state is dependent on the ligand density, the qualitative behavior as a function of substrate stiffness is independent of the ligand density (Fig. S3).

Integrin Particles and Implementation Algorithm. Integrin particles on the top surface diffuse in Brownian motion. At each time step of the simulation, the positions of each integrin particle, i, is updated, according to the Langevin equation of motion, with inertia negligible:

$$\boldsymbol{F_i} - \xi_i \frac{d\boldsymbol{r_i}}{dt} + \boldsymbol{F_i^T} = 0.$$

We used a time step $dt = 10^{-4}$ s and a friction $\zeta = 0.0142$ pN·s/μm, corresponding to a diffusion coefficient $D = 0.28\ \mu m^2/s$ (6), from:

$$\xi_i = \frac{k_B T}{D},$$

with $k_B T = 4.11$ pN·nm.

The force acting on integrin particles in the Langevin equation of motion has two contributions: a deterministic contribution and a stochastic contribution. The deterministic contribution comes from the tension of the bond toward the substrate and from the imposed velocity along xy:

$$\boldsymbol{F_i} = \boldsymbol{F_{sub}} + \boldsymbol{F_v}.$$

The stochastic contribution represents thermal fluctuations and obeys the fluctuation-dissipation theorem (8):

$$\left\langle \boldsymbol{F_i^T}(t)\boldsymbol{F_j^T}(t) \right\rangle = \frac{2k_B T \xi_i \delta_{ij}}{\Delta t}\boldsymbol{\delta},$$

where δ_{ij} is the Kronecker delta, and δ is a second-order tensor.

To integrate over time and update the positions of the various elements in the simulation, we use the explicit Euler integration scheme:

$$\boldsymbol{r_i}(t + \Delta t) = \boldsymbol{r_i}(t) + \frac{d\boldsymbol{r_i}}{dt}\Delta t = \boldsymbol{r_i}(t) + \frac{1}{\xi_i}\left(\boldsymbol{F_i} + \boldsymbol{F_i^T}\right)\Delta t.$$

Integrins can establish harmonic interactions with substrate springs, when in proximity of them, if the spring is free from a previous bond. Upon binding the substrate, integrin particles are subjected to a force parallel to the substrate, F_v, corresponding to a velocity of 1 nm/s, of the order of lamellipodium actin polymerization (9, 10).

The integrin/substrate interaction persists for a characteristic lifetime, τ, which depends upon the tension on the bond and follows the formalism of the implemented integrin unbinding rate, k_{off}.

A double exponential pathway determines unbinding rates, as a function of tension, f. It includes a strengthening pathway, with a negative exponent, and a weakening pathway, with a positive exponent. For wild-type conditions, the unbinding rate is:

$$k_{off} = 2e^{-0.064f} + 0.00005e^{0.288f}.$$

For Mn^{2+} conditions, the unbinding rate is:

$$k_{off} = 0.5e^{-0.0488f} + 0.00005e^{0.261f}.$$

The functional form of the catch bonds is taken from a model that assumes a single bound state and two unbinding pathways (11, 12) and was previously used for integrin-based adhesions (13). The coefficients of this form are estimated for reproducing maximum bond lifetime and corresponding tension from ref. 14 and integrin-unloaded affinity from refs. 15–17.

1. Yeung T, et al. (2005) Effects of substrate stiffness on cell morphology, cytoskeletal structure, and adhesion. *Cell Motil Cytoskeleton* 60:24–34.
2. Aratyn-Schaus Y, Oakes PW, Stricker J, Winter SP, Gardel ML (2010) Preparation of complaint matrices for quantifying cellular contraction. *J Vis Exp* (46):2173.
3. Tseng Q, et al. (2011) A new micropatterning method of soft substrates reveals that different tumorigenic signals can promote or reduce cell contraction levels. *Lab Chip* 11:2231–2240.
4. Oakes PW, Banerjee S, Marchetti MC, Gardel ML (2014) Geometry regulates traction stresses in adherent cells. *Biophys J* 107:825–833.
5. Sabass B, Gardel ML, Waterman CM, Schwarz US (2008) High resolution traction force microscopy based on experimental and computational advances. *Biophys J* 94: 207–220.
6. Rossier O, et al. (2012) Integrins β1 and β3 exhibit distinct dynamic nanoscale organizations inside focal adhesions. *Nat Cell Biol* 14:1057–1067.
7. Xu X-P, et al. (2016) Three-dimensional structures of full-length, membrane-embedded human α(IIb)β(3) integrin complexes. *Biophys J* 110:798–809.
8. Underhill PT, Doyle PS (2004) On the coarse-graining of polymers into bead-spring chains. *J Non-Newtonian Fluid Mech* 122:3–31.
9. Ponti A, Machacek M, Gupton SL, Waterman-Storer CM, Danuser G (2004) Two distinct actin networks drive the protrusion of migrating cells. *Science* 305:1782–1786.
10. Hotulainen P, Lappalainen P (2006) Stress fibers are generated by two distinct actin assembly mechanisms in motile cells. *J Cell Biol* 173:383–394.
11. Pereverzev YV, Prezhdo OV, Forero M, Sokurenko EV, Thomas WE (2005) The two-pathway model for the catch-slip transition in biological adhesion. *Biophys J* 89:1446–1454.

12. Pereverzev YV, Prezhdo OV, Thomas WE, Sokurenko EV (2005) Distinctive features of the biological catch bond in the jump-ramp force regime predicted by the two-pathway model. *Phys Rev E Stat Nonlin Soft Matter Phys* 72:010903.
13. Li Y, Bhimalapuram P, Dinner AR (2010) Model for how retrograde actin flow regulates adhesion traction stresses. *J Phys Condens Matter* 22:194113.
14. Kong F, García AJ, Mould AP, Humphries MJ, Zhu C (2009) Demonstration of catch bonds between an integrin and its ligand. *J Cell Biol* 185:1275–1284.
15. Gailit J, Ruoslahti E (1988) Regulation of the fibronectin receptor affinity by divalent cations. *J Biol Chem* 263:12927–12932.
16. Smith JW, Piotrowicz RS, Mathis D (1994) A mechanism for divalent cation regulation of beta 3-integrins. *J Biol Chem* 269:960–967.
17. Mould AP, Akiyama SK, Humphries MJ (1995) Regulation of integrin alpha 5 beta 1-fibronectin interactions by divalent cations. Evidence for distinct classes of binding sites for Mn2+, Mg2+, and Ca2+. *J Biol Chem* 270:26270–26277.

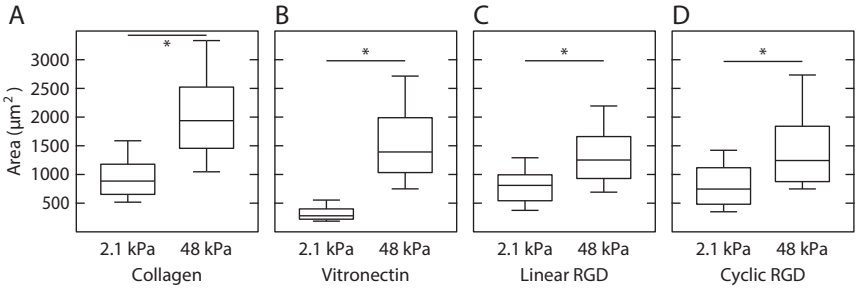

Fig. S1. Cell spread area in response to substrate stiffness is independent of ECM ligand. (*A*) Cells were plated on soft ($n = 240$) and stiff ($n = 255$) substrates coated with collagen. (*B*) Cells were plated on soft ($n = 74$) and stiff ($n = 55$) substrates coated with vitronectin. (*C*) Cells were plated on soft ($n = 137$) and stiff ($n = 150$) substrates coated with linear RGD peptide. (*D*) Cells were plated on soft ($n = 145$) and stiff ($n = 69$) substrates coated with cyclic RGD peptide. *$P < 0.01$.

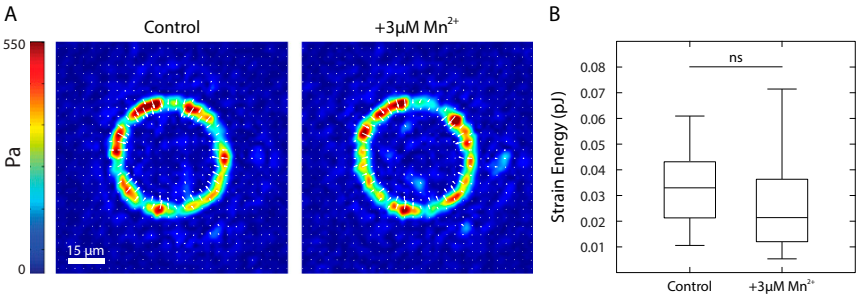

Fig. S2. Addition of Mn^{2+} does not directly affect cell contractility. (*A*) A representative cell traction map in control medium and the same cell after adding 3 μM Mn^{2+} for 30 min. The cell is plated on a circular micropattern of fibronectin to keep the cell from spreading further. The gel has a Young's modulus of ~8 kPa. No significant differences are seen between the two conditions. (*B*) The strain energy, or total contractile work done by the cell, for cells in control medium, and then the same cells after 30 min in media supplemented with 3 μM Mn^{2+}. All of the cells were fully spread out on circular micropatterns of fibronectin. No difference was seen between the two populations ($n = 20$). ns, not significant.

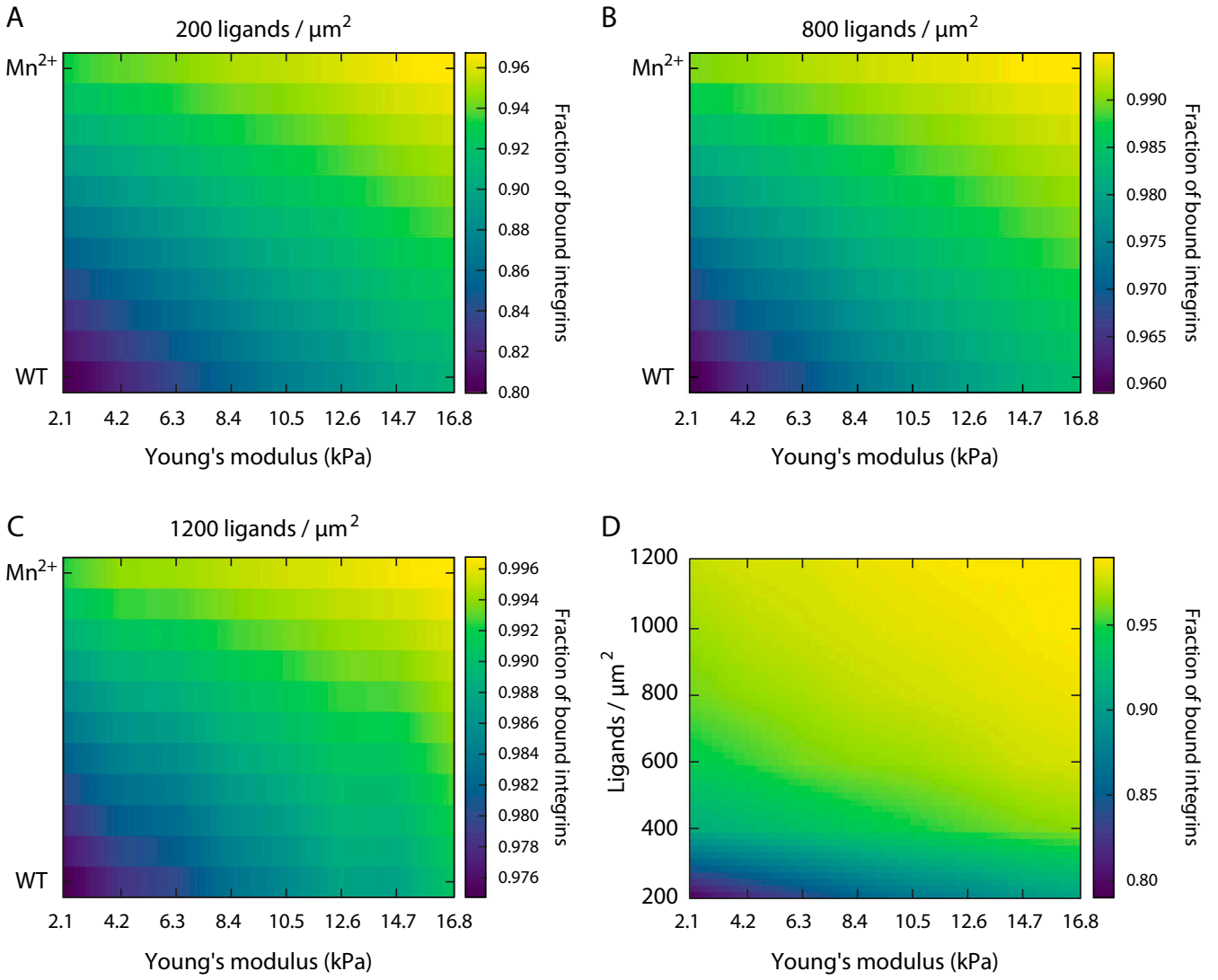

Fig. S3. Ligand density does not impact the relative effect of Mn^{2+}. (*A–C*) The average fraction of bound integrins for simulations of WT and Mn^{2+}-treated integrins as a function of substrate stiffness for 200 (*A*), 800 (*B*), and 1,200 (*C*) ligands per μm^2. (*D*) A phase map of the average fraction of bound integrins for WT integrins as a function of substrate stiffness and ligand density. For any given stiffness, the fraction of bound integrins increases with ligand density. Similarly, for any given ligand density, the fraction of bound integrins increases with substrate stiffness.

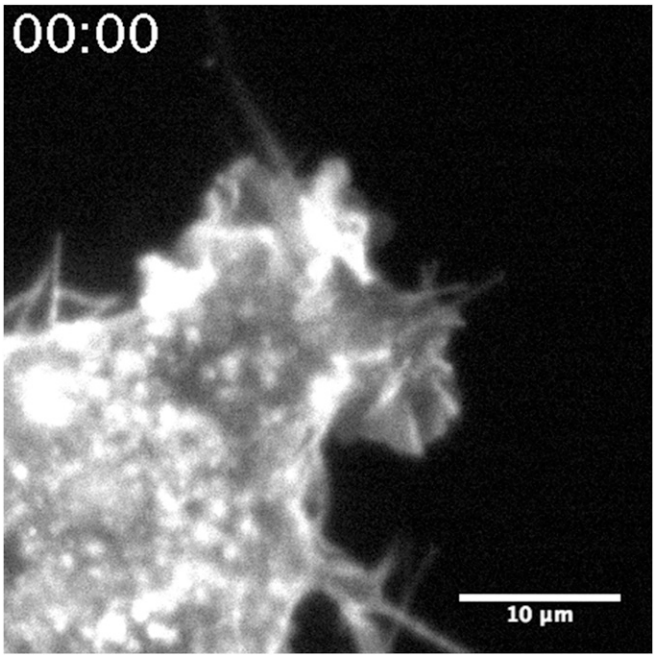

Movie S1. An NIH 3T3 fibroblast expressing a GFP membrane marker plated on a soft (2.1 kPa Young's modulus) substrate in the presence of 20 μM Y-27632. Time is in min:s. From Fig. 2*A*.

Movie S1

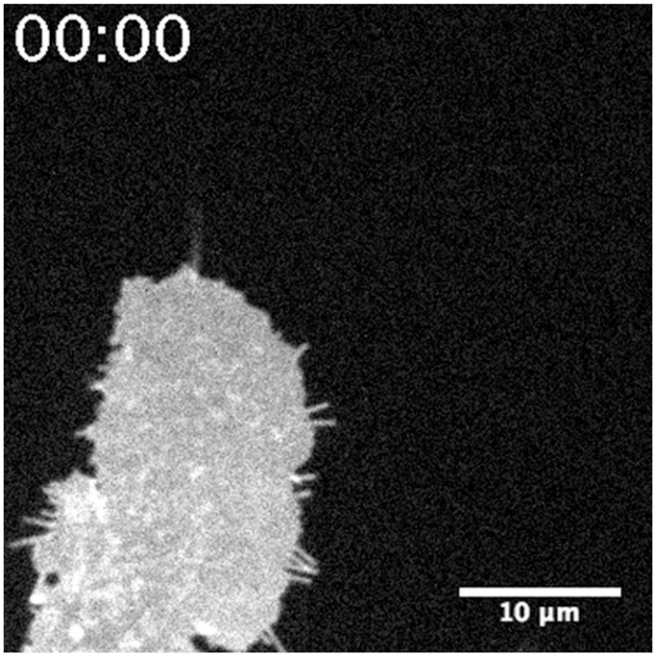

Movie S2. An NIH 3T3 fibroblast expressing a GFP membrane marker plated on a stiff (48 kPa Young's modulus) substrate in the presence of 20 μM Y-27632. Time is in min:s. From Fig. 2*B*.

Movie S2

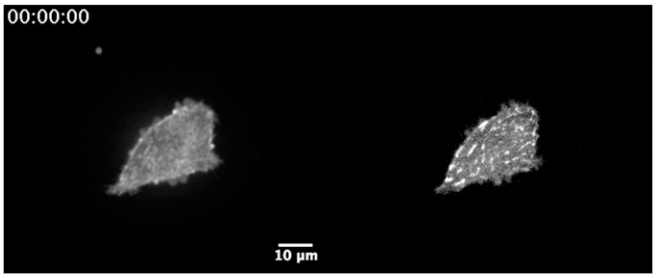

Movie S3. An NIH 3T3 fibroblast expressing mApple-actin and EGFP-paxillin plated on a soft (2.1 kPa young's modulus) substrate. AT ~20 min 3 μM Mn^{2+} is flowed into the imaging chamber. At ~80 min the Mn^{2+} is washed out of the chamber. Time is in h:min:s. From Fig. 4 *C* and *D*.

Movie S3